Drone-mounted GPR surveying: flight-height considerations for diffraction-based velocity analysis

Adam D Booth[1*] (a.d.booth@leeds.ac.uk), Tiffany M Koylass[1] (tiffany_mariah@hotmail.com)

1. Institute of Applied Geoscience, School of Earth and Environment, University of Leeds, Leeds, LS2 9JT, UK

* Corresponding author

Abstract

Recent studies highlight the potential of the drone platform for ground penetrating radar (GPR) surveying. Most guidance for optimising drone flight-heights is based on maximising the image quality of target responses, but no study yet considers the impact on diffraction travel-times. Strong GPR velocity contrasts across the air-ground interface introduce significant refraction effects that distort diffraction hyperbolae and introduce errors into diffraction-based velocity analysis. The severity of these errors is explored with synthetic GPR responses, using ray- and finite-difference approaches, and a real GPR dataset acquired over a sequence of diffracting features buried up to 1 m in the ground. Throughout, GPR antennas with 1000 MHz centre-frequency are raised from the ground to heights < 0.9 m (0-3 times the wavelength in air). Velocity estimates are within +10% of modelled values (spanning 0.07-0.13 m/ns) if the antenna height is within ½ wavelength of the ground surface. Greater heights reduce diffraction curvature, damaging velocity precision and masking diffractions against a background of subhorizontal reflectivity. Real GPR data highlight further problems of the drone-based platform, with data dominated by reverberations in the air-gap and reduced spatial resolution of wavelets at target depth. We suggest that a drone-based platform is unsuitable for diffraction-based velocity analysis, and any future drone surveys are benchmarked against ground-coupled datasets.

Keywords: GPR; drone; diffraction; velocity analysis

1. Introduction

Ground penetrating radar (GPR) is one of several geophysical systems to be considered for deployment on a drone-based platform. GPR is well established as a near-surface survey technique, using radio-wave energy to image a variety of geological, hydrological and anthropogenic targets in the upper few metres of the subsurface. Most often, the antennas of a GPR system remain in close contact with the ground surface but the growing availability and affordability of drone technology has prompted experimentation with drone-based GPR deployments.

Drones offer logistical advantages for applications involving rugged, dangerous and/or inaccessible terrains, e.g. over water courses (Lane Jr, 2019; Edemsky et al., 2021), at sites contaminated with unexploded ordnance (Cerquera, Montaño and Mondragón, 2017; García-Fernández et al., 2020; Šipoš and Gleich, 2020) or over crevassed glacier fields (Mankoff et al., 2020). Even for practical terrains, an autonomous drone following a pre-programmed flight path (Hammack et al., 2020) improves efficiency by allowing surveyors to deploy other equipment (e.g., systems that require manual installation such as seismic and/or resistivity methods). Although drone-based GPR surveys are subject to at least two sets of legislation, that regulate drone operations (e.g., Valentine, 2019) and GPR emissions (e.g., Ofcom, 2019), several recent studies have demonstrated advantages of the acquisition platform (Cerquera, Montaño and Mondragón, 2017; Chandra and Tanzi, 2018; Garcia-Fernandez et al., 2020; Edemsky et al., 2021).

When benchmarking against conventional ground-coupled deployments, assessments of drone-based GPR data typically consider the impact on recorded wavelet amplitudes. For air-launched systems, the GPR energy entering the subsurface is diminished by reflectivity losses at the air-ground interface (García-Fernández et al., 2020) but other factors vary as a function of the drone flight-height, and these include:

i) increased geometric spreading, with antennas positioned further from the target (García-Fernández et al., 2020);
ii) interference between reflections from the air-ground interface, and those from within the subsurface (Diamanti and Annan, 2017; Edemsky et al., 2021), and
iii) poorer spatial resolution given GPR beam spreading through air (Diamanti and Annan, 2017), and the vulnerability to artefacts from above-surface scatterers.

The experience of vehicle-mounted GPR surveys (e.g., Saarenketo and Scullion, 2000; Eriksen, Gascoyne and Al-Nuaimy, 2004; Zan et al., 2016) can provide a foundation for height considerations, but these often use horn antennas to maximise radiation in the target direction (usually

downwards). For any given centre-frequency, horn antennas tend to be bulkier than bow-tie systems (Pieraccini, Rohjani and Miccinesi, 2017) hence, with accompanying batteries and control units, may exceed the payload of the drone. Furthermore, most experiments with drone-based GPR aim to mount an existing commercial system on the drone and most of these have a bow-tie design. The issues listed above may therefore represent widespread design considerations, but recommendations for flight-height remain disparate, variously suggesting flying at any height between 0.5-1.5 times the dominant wavelength of the radar wavelet (e.g., Diamanti and Annan, 2017; García-Fernández et al., 2018, 2020; Šipoš and Gleich, 2020).

Having noted these amplitude effects and the research effort to understand them, this paper investigates the impact of flight-height on travel-time relationships expressed in recorded data and how they impact diffraction-based velocity analysis. A starting assumption, when comparing to ground-based data, may be that reflections in drone-based data are simply shifted late according to the additional travel-time through the air gap. This may be reasonable for specular reflectivity, but refraction effects at the air-ground interface can cause distortions to the appearance of diffraction hyperbolae (Causse, 2004). This is especially problematic for (e.g.) engineering and archaeological applications where targets are often detected using diffraction responses and, furthermore, their curvature is used to determine subsurface velocities (e.g., for migration and depth conversion). Velocities may also be converted to dielectric permittivity, to inform derivative quantities such as water content (Bradford et al., 2009; St Clair and Holbrook, 2017). The limitations of hyperbolic velocity analysis, and the equivalent issues in seismic reflection processing (e.g., Alkhalifah, 1997), will be familiar to many in the community but, to date, there has been no study to explore the magnitude of velocity errors for a drone-based GPR system. It is therefore worth exploring the feasibility of diffraction-based velocity analysis for this novel survey platform.

Using ray-based and finite-difference synthetic analyses, we show the severity of these distortions as the height of drone-mounted antennas is changed, and demonstrate the impact on diffraction-based velocity analysis. Our synthetics are complemented with a real-data representation of drone acquisition, with antennas mounted on a height-adjustable frame. Finally, we advise on the situations in which ‘fly low’ or ‘fly high’ approaches may be preferable.

2. Diffraction travel-times and velocity relationships

The travel-time, t, of a diffraction hyperbola from a point-source target is

$$t = \sqrt{t_0^2 + \frac{4(x-x_0)^2}{v_{RMS}^2}} \quad (1)$$

where x is the midpoint position between common-offset GPR antennas, x_0 is the surface position vertically above the diffractor, t_0 is the two-way travel-time of diffracted arrivals at x_0, and v_{RMS} is root-mean-square velocity. Assuming that drone-mounted antennas are flown at height h above a subsurface with constant velocity v_{sub}, v_{RMS} is the travel-time weighted average between v_{sub} and the velocity of the GPR wavelet through air (v_{air}, = 0.3 m/ns):

$$v_{RMS} = \sqrt{\frac{v_{sub}^2(t_0-t_{air})+v_{air}^2 t_{air}}{t_0}}, \quad (2)$$

where t_{air} is the two-way travel-time (= $2h/v_{air}$) through the air-gap at $x = x_0$. For a ground-based system, t_{air} is 0 and $v_{RMS} = v_{sub}$. These equations are strictly valid for monostatic systems, with zero transmitter-receiver offset, but nonetheless remain widely applied for finite-offset bistatic systems.

v_{RMS} can be evaluated using several analytic methods, including curve-fitting approaches and semblance-based velocity analysis (Booth and Pringle, 2016). With pairs of v_{RMS} and t_0 available, v_{sub} can be approximated using Dix's Equation (Dix, 1955):

$$v_{sub} \approx \sqrt{\frac{v_{RMS}^2 t_0 - v_{air}^2 t_{air}}{t_0 - t_{air}}}, \quad (3)$$

which can be used recursively to derive the vertical variation of v_{sub} if v_{RMS}:t_0 pairs are available.

Equation (1) is exactly hyperbolic for ground-based systems and constant, isotropic, v_{sub},. In layered velocity models, non-hyperbolic travel-time terms are introduced because refraction across interfaces is neglected. Since travel-times deviate from those predicted by Equation (1), velocity estimates derived with it are inaccurate with respect to true v_{sub}. This is exacerbated where $|x\text{-}x_0|$ is large with respect to the vertical distance between the antennas and the target (i.e., the sum of flight-height and target depth). These errors can be circumvented using higher-order terms in travel-time approximations (e.g., Causse, 2004; Causse and Sénéchal, 2006) or through full waveform inversion (e.g., Jazayeri et al., 2018), but these are less widespread in practice than assuming hyperbolic travel-times and accepting some velocity error. However, strong refraction across the air-ground likely increases the severity of these errors.

Additionally, there are systematic velocity errors that should be considered for any practical velocity analysis. A diffracting target with a finite radius causes v_{sub} to be biased fast (Shihab and Al-Nauimy,

2005; Ristic et al., 2009) and v_{sub} is exaggerated further if the intersection between the long-axis of an elongate diffractor (e.g., a pipe) and the profile direction is not orthogonal. Conversely, many velocity analysis approaches (e.g., curve-matching and semblance) consider the travel-times of the highest amplitude cycles of the GPR wavelet and therefore cause v_{sub} to be biased slow; velocity is expressed more accurately by first-breaks travel-times (Booth, Clark and Murray, 2010; Booth and Pringle, 2016). Although the impact of these is appreciated, the relative significance of velocity errors from a drone-based survey platform is currently unexplored.

3. Data Simulation

Two approaches were adopted to simulate drone-mounted GPR acquisitions, using different flight heights and a range of v_{sub}. First, ray-tracing was used to illustrate the distortion of diffracted raypaths. Second, finite-difference models were implemented in gprMax, to capture the near-field behaviour of a finite-frequency wavefield and a more realistic antenna radiation pattern.

3.1 Ray-based synthetics

Travel-times were computed for a point diffractor at 0.2 m depth in a homogeneous isotropic half-space. Bistatic transmitting and receiving antennas were offset at 0.02 m, and midpoint positions extended to ±0.5 m either side of the diffractor, sampling every 0.02 m. Responses were modelled with drone flight-height, h, ranging from 0 to 0.9 m (i.e., up to 3-times the wavelength in air, λ, of the 1000 MHz wavelet used in later synthetics and field survey). v_{sub} was increasing in 0.01 m/ns increments from 0.07-0.13 m/ns.

Figure 1 shows modelled raypaths for all h and v_{sub} = 0.09 m/ns. The ground-based model (Figure 1a) shows the straight-rays expected for constant v_{sub}, but low drone flight-heights introduce significant ray-bending across the air-ground interface which gradually decreases with increasing h. The corresponding travel-time curves (Figure 2a) highlight the distortion from the diffraction hyperbola recorded by ground-based antennas. For models with h > 0, the ground-going leg of the raypaths shows little variation from the vertical, hence the corresponding diffractions are simply time-shifted variants of a hyperbola originating at the air-ground interface. In all cases, the shift is ~ 4.4 ns, corresponding to the vertical two-way travel time between the air-ground interface and the diffractor. This implies that refraction effects prevent v_{sub} from significantly influencing the curvature of the diffraction response.

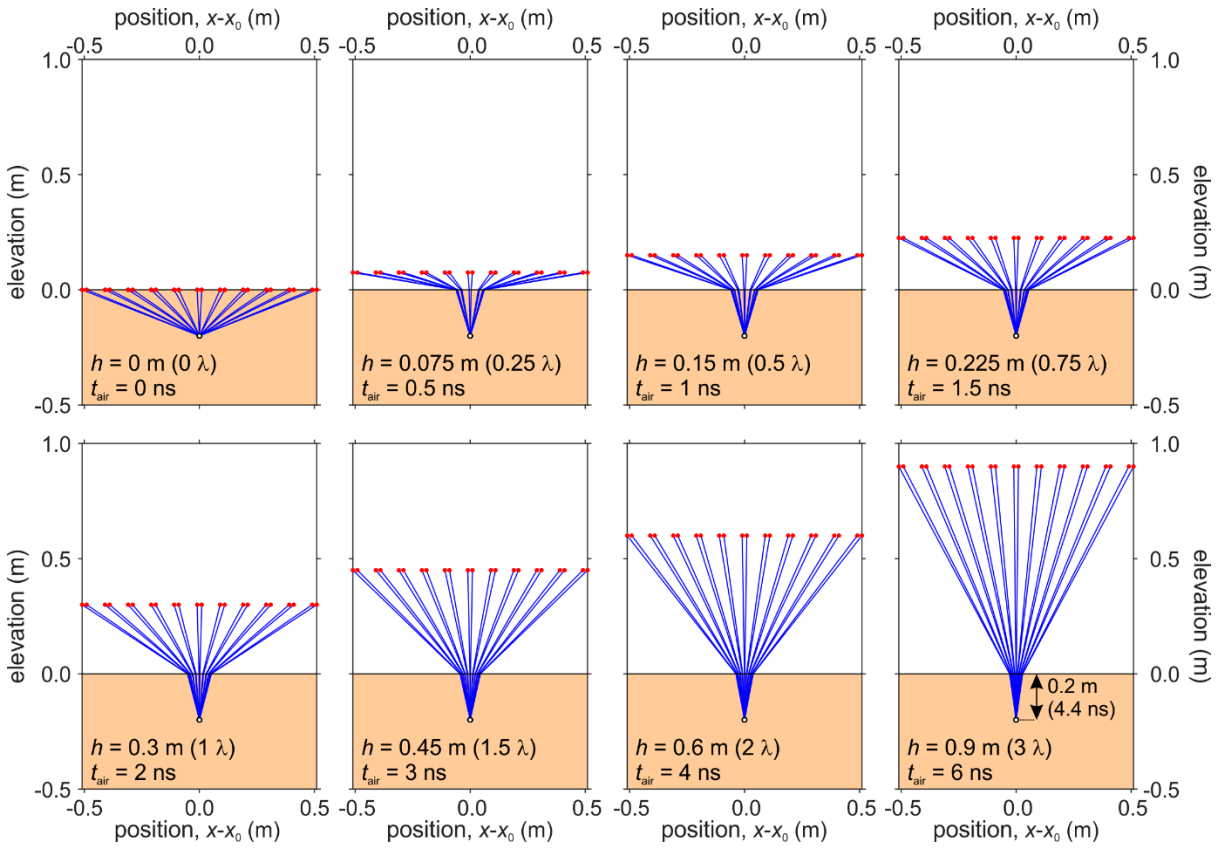

Figure 1. Raypaths modelled for a point diffractor, placed at 0.2 m depth in a subsurface with constant v_{sub} = 0.09 m/ns. Each panel shows antennas (red circles) raised to successively increased height, from 0 to 0.9 m, and the corresponding t_{air}. The additional annotation in the lower-right panel shows the vertical travel-time, 4.4 ns, between the diffractor and ground surface.

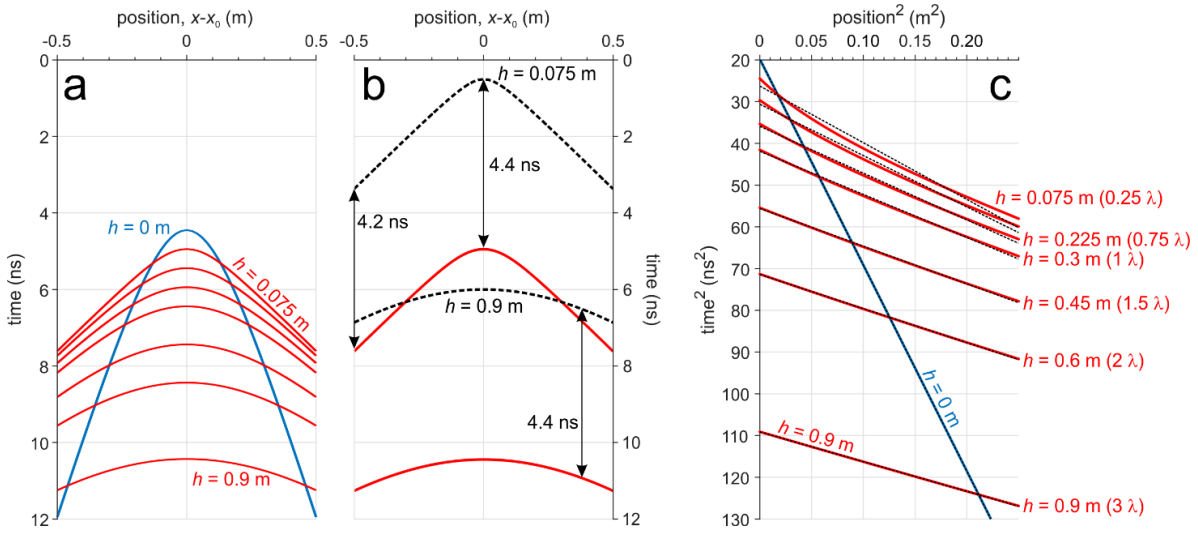

Figure 2. Ray-based travel-time curves for models in Figure 1. a) Curves for ground-based (blue; $h = 0$) and airborne (red; $h > 0$) antennas. b) End-member curves from (a), compared to diffraction hyperbolae (black dashed lines) from a diffracting target placed at the ground surface. Each pair of curves is simply shifted by ~4.4 ns. c) Expression of curves in (a) on t^2-x^2 axes, and best-fit straight-lines (black dashed lines) for each.

v_{RMS} is estimated for each model using a linear regression to diffraction travel-times, expressed in Figure 2c on t^2-x^2 axes. The reciprocal gradient of the best-fit straight-line (black dashed lines) defines $½v_{RMS}^2$, and its intercept t_0^2. Being exactly hyperbolic, travel-times for ground-based antennas are fit perfectly, however non-hyperbolic terms for $h > 0$ introduce curved t^2-x^2 responses which are most evident for $h \leq 0.3$ m. v_{sub} was estimated for each case by substituting v_{RMS}:t_0 into Dix's Equation, together with t_{air} (annotated in Figure 1) and v_{air} = 0.3 m/ns. Figure 3a shows v_{RMS} and the resulting v_{sub}, the latter expressed as a percentage error in Figure 3b.

All v_{sub} estimates are biased fast but the largest errors are shown for the lowest h (e.g., 70% overestimate for h = 0.075 m, 14% for h = 0.9 m). Equivalent overestimates for all modelled v_{sub} (Figure 3c) suggest that velocity mismatch decreases with both increasing h and v_{sub}. For the fastest velocity case, overestimates are always < 40%, and are ~7% for the highest flight-heights. However, overestimates can approach 100% for cases of $v_{sub} \leq 0.08$ m/ns and low flight-heights.

The analysis was repeated for diffractors placed at 0.6 m and 1.0 m depth (Figures 3d and e, respectively). For the 0.6 m case, v_{sub} overestimates are typically < 20%, improving to < 10% with faster v_{sub} and/or greater flight-height. The overestimate seldom exceeds 10% for the 1 m-deep case, but targets at this depth would not widely be considered suitable for imaging with 1000 MHz antennas. The errors in Figure 3b are therefore more illustrative of a typical best-case scenario.

3.2 Finite-difference synthetics

Ray-based modelling illustrates the challenges for diffraction-based velocity analysis but neglects realistic aspects of GPR propagation. As ray-based synthetics are infinite-frequency models, they impose far-field conditions and thus plane-wave arrivals, yet shallow targets could be present in the near-field (e.g., within a small number of wavelengths; Warren and Giannopoulos, 2012) where wavefront curvature is significant. Furthermore, ray-based arrivals were weighted equally in the linear regression, whereas amplitudes in real data are affected by changes in ray length due to geometrical spreading, attenuation losses and, in particular, the anisotropic radiation pattern of GPR antennas. The lattermost is likely to be particularly significant given the obliquity of the far-offset raypaths implied for low-h in Figure 1.

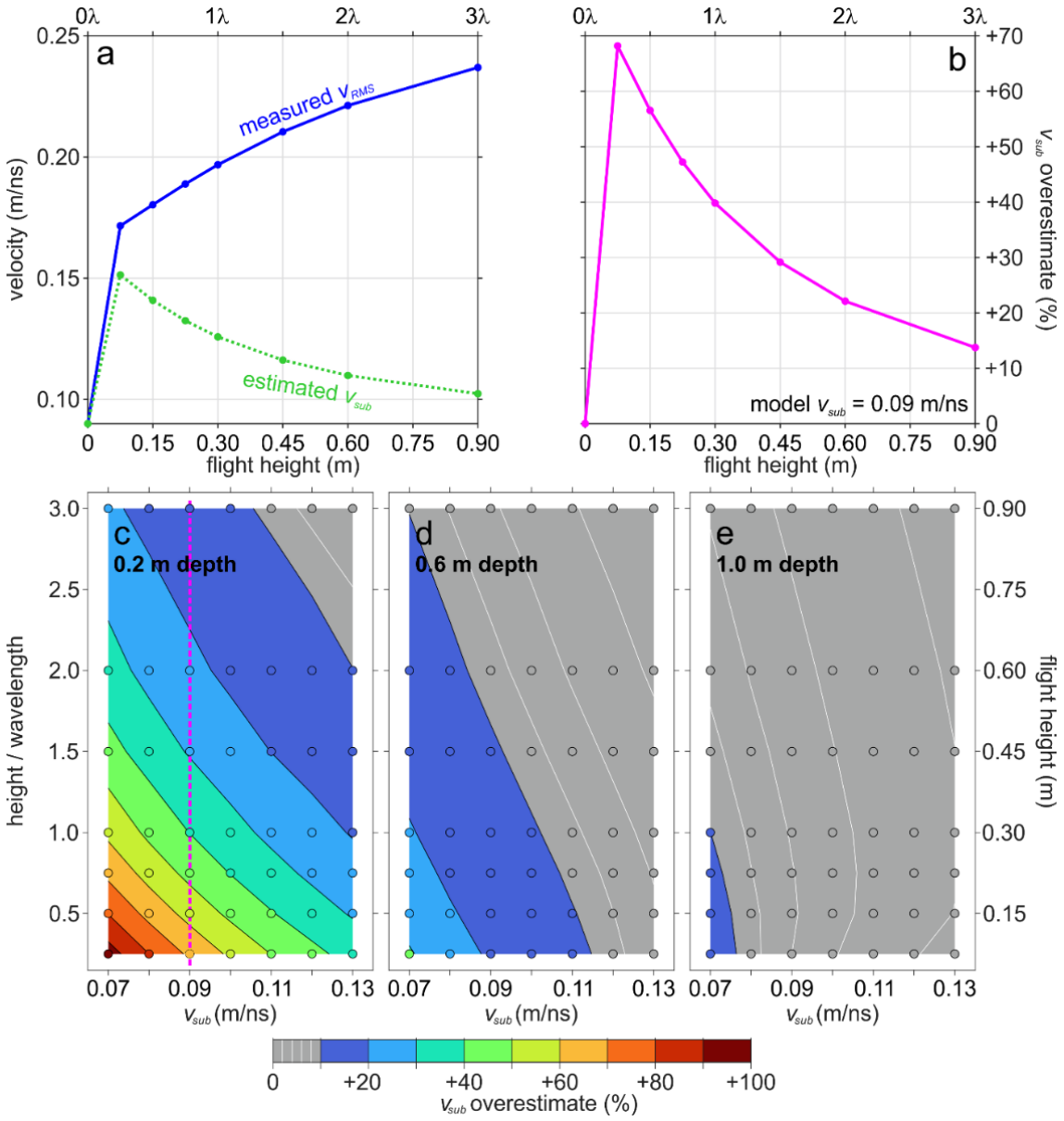

Figure 3. Measured velocities and errors with changing flight-height. a) v_{RMS} measured from t^2-x^2 analysis (solid, blue), and the estimated v_{sub} (dashed, green) after substitution into Dix's Equation. b) Percentage overestimate of v_{sub}, with respect to model value of 0.09 m/ns. c-e) Overestimates of a range of v_{sub} values for point diffractors at 0.2 m, 0.6 m and 1.0 m depth respectively. Contours are filled at 10% intervals, with white contours appearing at intervals of 2% within the 0-10% range. The pink dashed line in (c) corresponds to the data in (b).

Finite-difference synthetics were undertaken using gprMax (Warren, Giannapoulos and Giannakis, 2016). A 3-D domain of dimension [x, y, z] = [1.0 x 1.0 x 1.2] m was established and discretised into cells of dimension [Δx, Δy, Δz] = 0.005 m. The modelled structure is 2.5D, continuous in the y-dimension and represents a horizontal pipe installed in a trench (Figure 4). The pipe is a cylindrical perfect electrical conductor (pec), with diameter 0.1 m and centred at [x, z] = [0.5, 0.2] m. The horizontal floor of the trench is 0.5 m wide, 0.3 m deep, and rises to 0.2 m at the edges of the

domain. The overlying air-gap extends 0.7 m above the ground surface, allowing antennas (red circles, Figure 4) to be placed at a range of h from 0 to 0.6 m. This is up to 2 λ, for the 1000 MHz source wavelet we assumed.

All physical quantities are fixed, except for the relative dielectric permittivity, ε_r, of the trench fill which is first set to 18.3 and then to 5.3, giving v_{sub} of 0.07 and 0.13 m/ns (the extreme velocity cases considered in Section 3.1). The velocity through the lowermost layer is fixed at 0.010 m/ns, such that the velocity contrast at the base of the trench is ± 0.03 m/ns. Output radargrams were made at y = 0.5 m, with antenna midpoints spanning 0.05-0.95 m, in 0.02 m intervals. The time step in these was downsampled, from 0.0096 ns, to 0.1 ns via linear interpolation. The radargrams were contaminated with noise traces from a 1000 MHz field dataset (Section 4), scaled to give 15 dB signal-to-noise ratio at the diffraction apex.

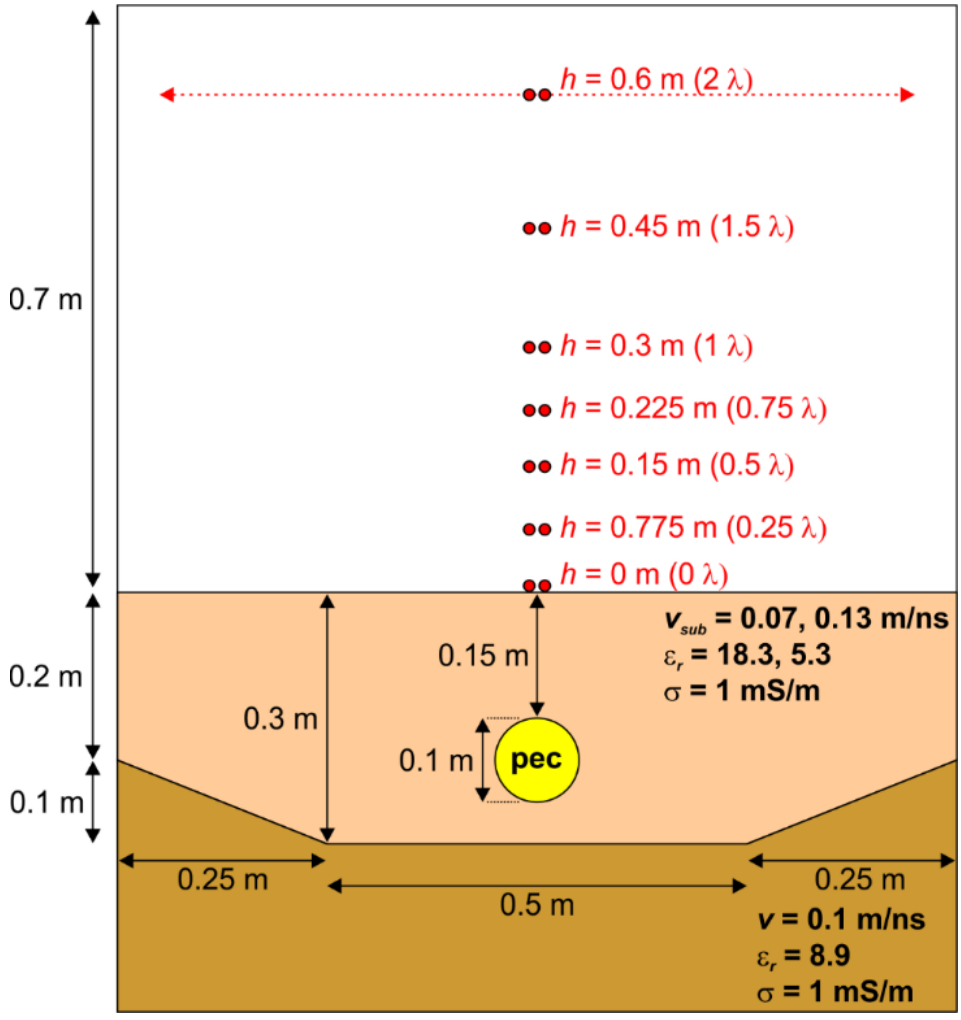

Figure 4. [x,z] cross-section through the gprMax model. A cylindrical perfect electric conductor (pec) is placed at 0.15 m depth in a subsurface with fixed electrical conductivity (σ = 1 mS/m) but variable v_{sub}. Antennas (red circles) span a range of x from 0.05 to 0.95 m, and are positioned at h up to 0.6 m (0-2λ).

Velocity analysis was undertaken for each model using semblance (e.g., Stucchi et al., 2020), configured using the travel-time expression in Equation (1) (Booth and Pringle, 2016). The calculation spanned an aperture of 0.4 m either side of the apex and used an analysis window with 0.1 ns duration. Figure 5 shows output radargrams and their semblance responses; columns (a) and (b) relate to v_{sub} of 0.07 m/ns and 0.13 m/ns, respectively, with rows (i) to (vii) showing flight-heights increased from 0 to 0.6 m. The hyperbola on each radargram is the semblance-derived approximation to first-break travel-times (ornament ⊕). These are based on semblance picks made at the strongest semblance response, corresponding to the strongest half-cycle of the GPR wavelet (ornament ⊗) but corrected for the ~0.53 ns lag from first break (Booth, Clark and Murray, 2010). The precision in v_{RMS}, and in v_{sub} thereafter, is based on the width of the 90% semblance contour (Booth, Clark and Murray, 2011).

Diffraction responses in Figure 5 flatten progressively with increasing h, becoming indistinct from the response from the trench floor. Furthermore, consistent with observations in Figure 2b, they become time-shifted replicas of each other: the travel-time moveout of the diffractions differs by just 0.8 ns between panels aviii and bviii, despite the difference in the velocity models. Figure 6 shows that v_{RMS} tends towards 0.3 m/ns as h increases (Figure 6a,c), with both v_{RMS} and v_{sub} becoming increasingly imprecise. For expressing v_{sub} as a fractional error (Figure 6b,d), reference values are increased respectively to 0.079 m/ns and 0.134 m/ns to incorporate the finite-radius effect of our pipe geometry: with a radius-to-centre-depth ratio of 0.25, these increases are consistent with those shown by Shihab and Al-Nuaimy (2005). For comparison, Figures 6b and d also include the relative errors in v_{sub} from the ray-based models in Figure 3a.

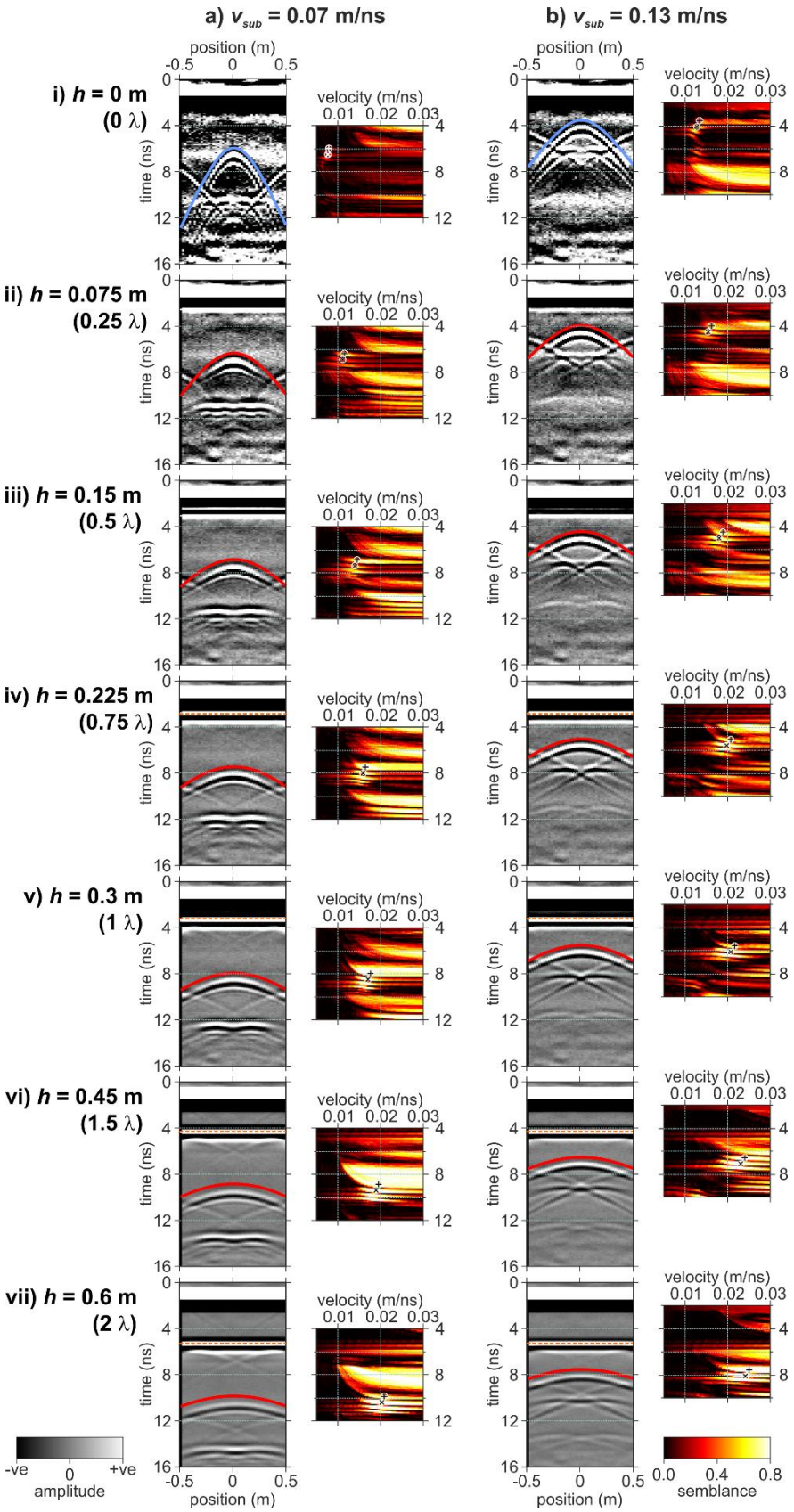

Figure 5. Synthetic radargrams and semblance responses for v_{sub} of a) 0.07 m/ns and b) 0.13 m/ns, and h increased (i to vii) from 0 to 0.6 m. The hyperbola in each radargram approximates first-break travel-times using semblance picks corrected (ornament ⊕) from peak responses (ornament ⊗). Orange dashed line in models with h > 0.15 m shows the reflection from the air-ground interface. All radargram and semblance panels share the same colour scale and amplitude range.

Although Figure 6 suggests that model v_{sub} will be overestimated for any h > 0, errors are generally less than in ray-based models particularly for small h. For h = 0.075 m (0.25 λ), ray-based models indicated that slow velocities could be overestimated by 100%, yet Figure 6b suggests an overestimate no greater than ~5%. This is attributed to antenna radiation effects, which truncate the effective offset-to-depth ratio over which diffractions can contribute to the semblance analysis. For ε_r > 12, Warren and Giannopolous (2012) indicate a reduction of > 20 dB in radiated amplitudes for take-off angles exceeding 60°. For our model geometry and h = 0.075 m, this angle is reached when antennas are located ± 0.16 m either side of the diffractor. The effect is clear in Figure 6aii, in which diffracted amplitudes decrease rapidly beyond positions ± 0.2 m from the diffraction apex. Likewise, the semblance-defined hyperbola best describes the diffraction curvature around the apex. Indeed, in revisiting Figure 2c, the local gradient of the h = 0.075 m curve is steepest in the $[0\text{-}0.2]^2$ m^2 range of x^2, and a linear regression using only this range reduces the overestimate of v_{sub} from ~100% to ~45%. However, a velocity analysis strategy that instead draws on manually or automatically defined travel-time picks (e.g., Dou et al., 2017) would remain vulnerable to non-hyperbolic effects if the positional range was unrestricted.

Guidance from finite-difference simulations is therefore opposite to ray-based modelling, indicating that the accuracy *and* precision of velocity estimates is benefitted by a low flight-height. Furthermore, given their flatness, the responses observed with antennas > 0.3 m (1 λ) high are likely more vulnerable to noise and static shifts resulting from velocity heterogeneity and or antenna mispositioning.

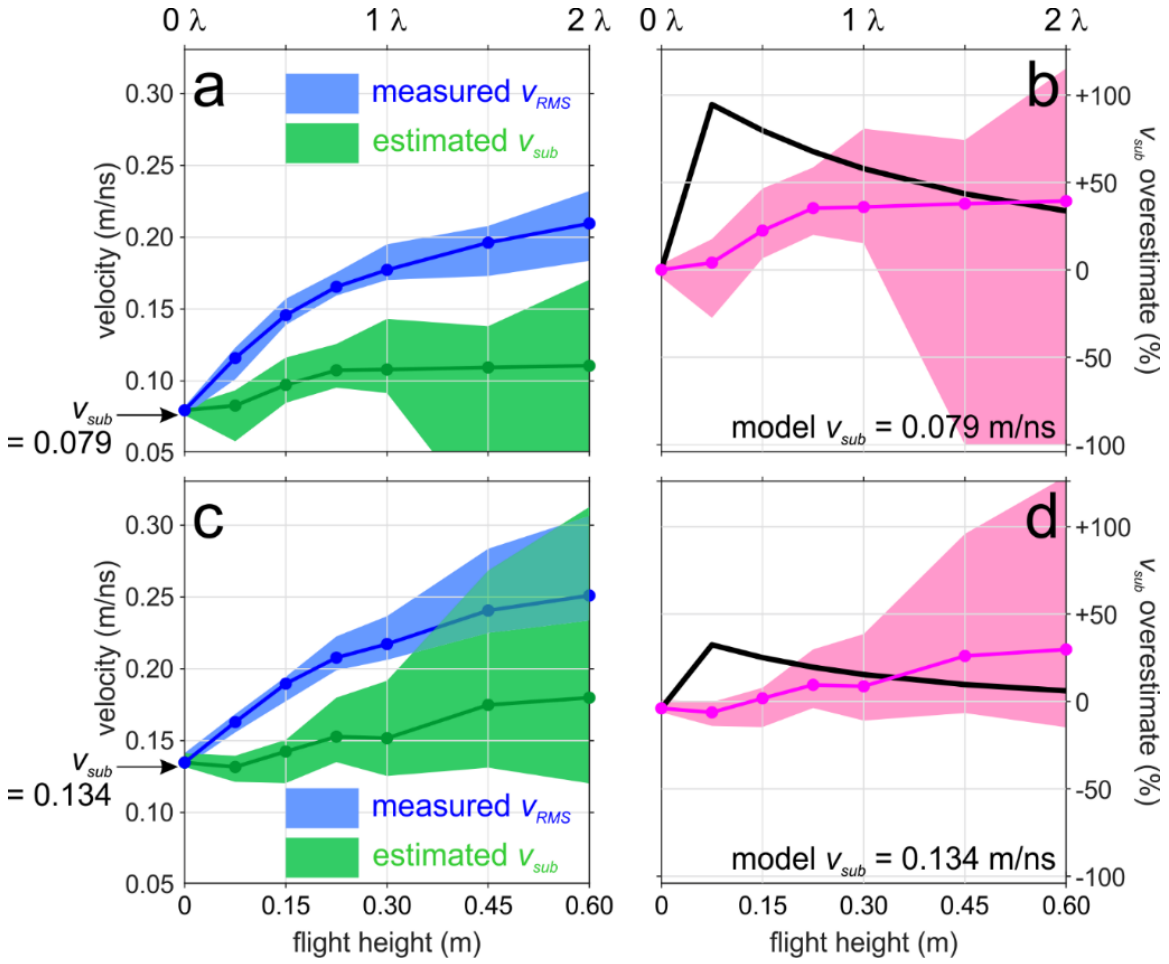

Figure 6. Semblance-derived v_{RMS} and v_{sub} for the models in Figure 6. Coloured areas show velocity estimates and their precision for (blue) v_{RMS} and (green) modified v_{sub} of (a,b) 0.079 m/ns and (c,d) 0.134 m/ns. Pink areas in b and d show the percentage overestimate in model v_{sub}, with black lines showing the equivalent errors from ray-based models in Figure 3c.

4. Field data

The practical implications of the synthetic models were explored using GPR field data, acquired with an adaptable frame to simulate drone-based acquisitions at varying flight-heights (Figure 7a). The frame is made from a polystyrene cradle and carries Sensors&Software (S&S) pulseEKKO PRO 1000 MHz antennas with 0.15 m offset between antenna centres. Consistent with a drone platform, there is no material beneath the antennas hence they radiate directly into the air. A carry handle from a S&S low-frequency antenna is attached to the frame with its adjustable legs marked in 0.05 m intervals. With the system carried at a constant level, the antennas can be elevated to different heights above the ground surface. Along-profile distances were measured using a calibrated odometer wheel, towed behind the frame.

Field data (Booth, 2021) were acquired in July 2020 on Canal Road (UK National Grid SE 22306 36370), a quiet side-street in the Rodley district of Leeds, UK (Figure 7b). Restrictions imposed during the UK's COVID-19 response limited the range of accessible field locations. Nonetheless, Canal Road is of archaeological interest given its 200-year history accessing an industrial wharf on the adjacent Leeds-Liverpool canal (Figure 7b): the modern road surface likely covers the original structure.

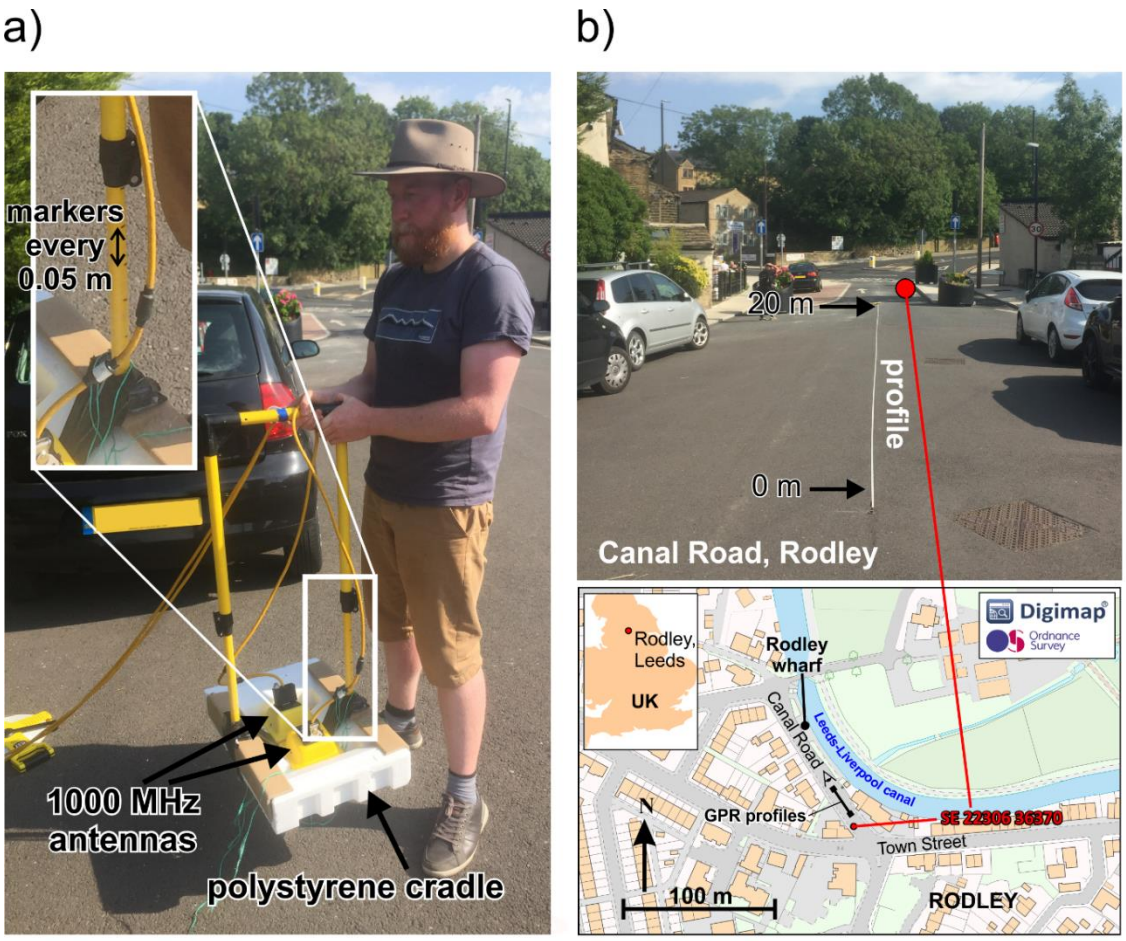

Figure 7. Field data acquisition. a) 1000 MHz antennas placed within a polystyrene frame, to simulate drone-mounted GPR surveys. Inset, markers to simulate different flight-heights. b) Survey location on Canal Road, Rodley, UK. Upper: view south-east along Canal Road and the position of 20 m-long profiles. Lower: Site map from UK Ordnance Survey showing Canal Road and its proximity to the Leeds-Liverpool canal and a defunct wharf. Viewpoint for upper panel is marked.

GPR profiles are 20 m long, although only their first 8 m are used in this paper, with 0.01 m trace interval and repeated with h increasing from 0 to 0.35 m in increments of 0.05 m (= $\lambda/6$ for a 1000 MHz wavelet in air). The time sampling internal was 0.1 ns. Data were processed in Sandmeier ReflexW© software (version 8.5), using the sequence:

i) dewow filter (window length 2 ns),

ii) Ormsby bandpass filter (corner frequencies at 200-400-1200-2400 MHz),

iii) time-variant 'energy decay' gain function, and

iv) spatial filtering (3 m window).

The noise traces with which the gprMax models (Figure 5) were contaminated are extracted from 13-20 ns in the ground-based profiles.

The ground-based acquisition (Figure 8a) revealed a sequence of sub-horizontal interfaces and a series of diffractions with a regularly spacing of 0.5-0.6 m intervals, rising from ~8 ns to ~6 ns travel-time through the profile. Although their origin is unknown, presumed to related to the original road foundation, they nonetheless provide targets for diffraction-based velocity analysis.

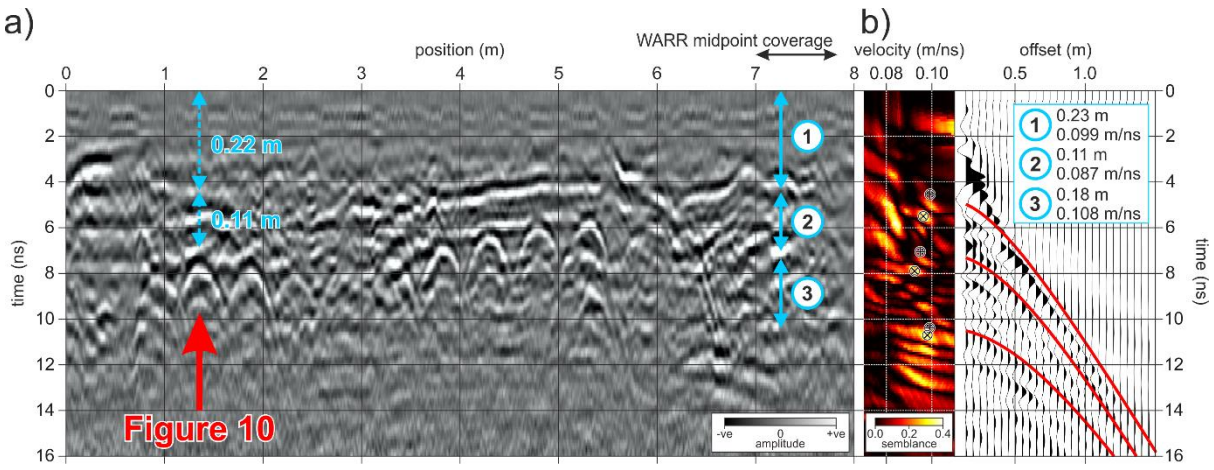

Figure 8. Ground-based GPR data from Canal Road surveys. a) First 8 m of ground-based GPR profile. A diffraction at 1.35 m position (~ 0.33 m depth, beneath subhorizontal layering) is highlighted for later analysis. b) WARR data, spanning a midpoint range of 7.0-7.8 m, and its semblance response. Reflection hyperbolae (red) are defined by [v_{RMS}:t_0] shown by ornament ⊕ in the semblance panel. Inset: three-layer velocity:thickness model, accurate to ~ ±15%, based on the 90% semblance contour.

A wide-angle reflection/refraction (WARR) survey (Annan and Jackson, 2017; Figure 8b) was acquired to provide velocity control: the transmitter was located 6.90 m along the profile, with the receiver position moved in 0.05 m increments from 7.05 to 8.65 m (0.15-1.85 m offset range). The semblance response to the WARR data suggests a three-layer velocity model (inset, Figure 8b). On substituting corrected semblance picks (ornament ⊕) into Dix's Equation and extrapolating the resulting velocity model across the profile, the deepest clear diffraction (position 1.35 m, marked with the red arrow) is interpreted to originate from the base of a layer at 0.33 ± 0.05 m depth, 0.11 ±

0.05 m thick, with v_{sub} = 0.087 ± 0.008 m/ns. This v_{sub} is used as the reference velocity, against which velocity errors are later compared, although it is acknowledged that ground truth velocities and diffractor geometries are unknown.

Recorded profiles are shown in Figure 9, displayed before (8a) and after (8b) the application of spatial filtering. For $h \geq 0.1$ m ($2\lambda/6$; 8aiii-vii), data are dominated by horizontal ringing, assumed to be reverberations between the ground surface (marked in Figure 8b) and the base of the antennas. Perturbations in the travel-time of the surface reflection suggest some inconsistency in the antennas' height, but these are typically < 0.2 ns (< 0.03 m) and are therefore negligible at target depth (and, in any case, may be representative of the stability of a real drone platform). The reverberations are suppressed with the application of spatial filtering, but the subsurface structure remains greatly obscured for h ≥ 0.1 m ($2\lambda/6$). For $h \geq 0.1$ m (1λ), some expression of the subhorizontal layering appears (e.g., at ~10 ns in Figure 8bvi) but the diffractions remain obscured, and the image would be difficult to interpret without also seeing the ground-based data.

With the sparsity of available diffraction responses in the field data, velocity analysis was only performed for the diffraction at 1.35 m along the profile, for ground-based antennas and h = 0.05 m (Figures 10a and b, respectively). Semblance is calculated in a 0.1 ns window and spans an aperture of 0.25 m either side of the diffraction apex. As anticipated, the air gap increases v_{RMS}. The 13% increase (from v_{RMS} of 0.0917 m/ns, to 0.104 m/ns) is approximately half of that suggested in Figure 6c for representative flight heights but the behaviour of the real data is more consistent with the finite-difference synthetics than their ray-based equivalent.

The accuracy of v_{sub} estimates is compared against the reference model at 1.35 m (Figure 8). For the ground-based data, v_{RMS} and t_0 through the overburden are 0.099 m/ns and 4.4 ns respectively. Combining these in Dix's Equation with the quantities derived in Figure 10a, v_{sub} is estimated as 0.077 ± 0.003 m/ns, within 13% of the model v_{sub}. For h = 0.05 m, the overburden v_{RMS} must first be recalculated to allow for propagation through the air-gap. Using Equation (2), and assuming t_{air} = 0.33 ns (= $2h/v_{air}$), the [v_{RMS}:t_0] pair at the base of the first subsurface layer is [0.127 m/ns, 4.77 ns]. Here, Dix's Equation yields an implausibly slow v_{sub} estimate of 0.036 m/ns, although this is highly sensitive to uncertainty ranges: when v_{RMS} is increased by 0.009 m/ns to its upper uncertainty bound, the implied v_{sub} is increased to 0.085 m/ns. Dix's Equation is vulnerable to uncertainties particularly where travel-time differences in the denominator of the expression are small. However, this is exacerbated for drone-based surveying, where the addition of an air-gap adds further measurement uncertainty to the analysis.

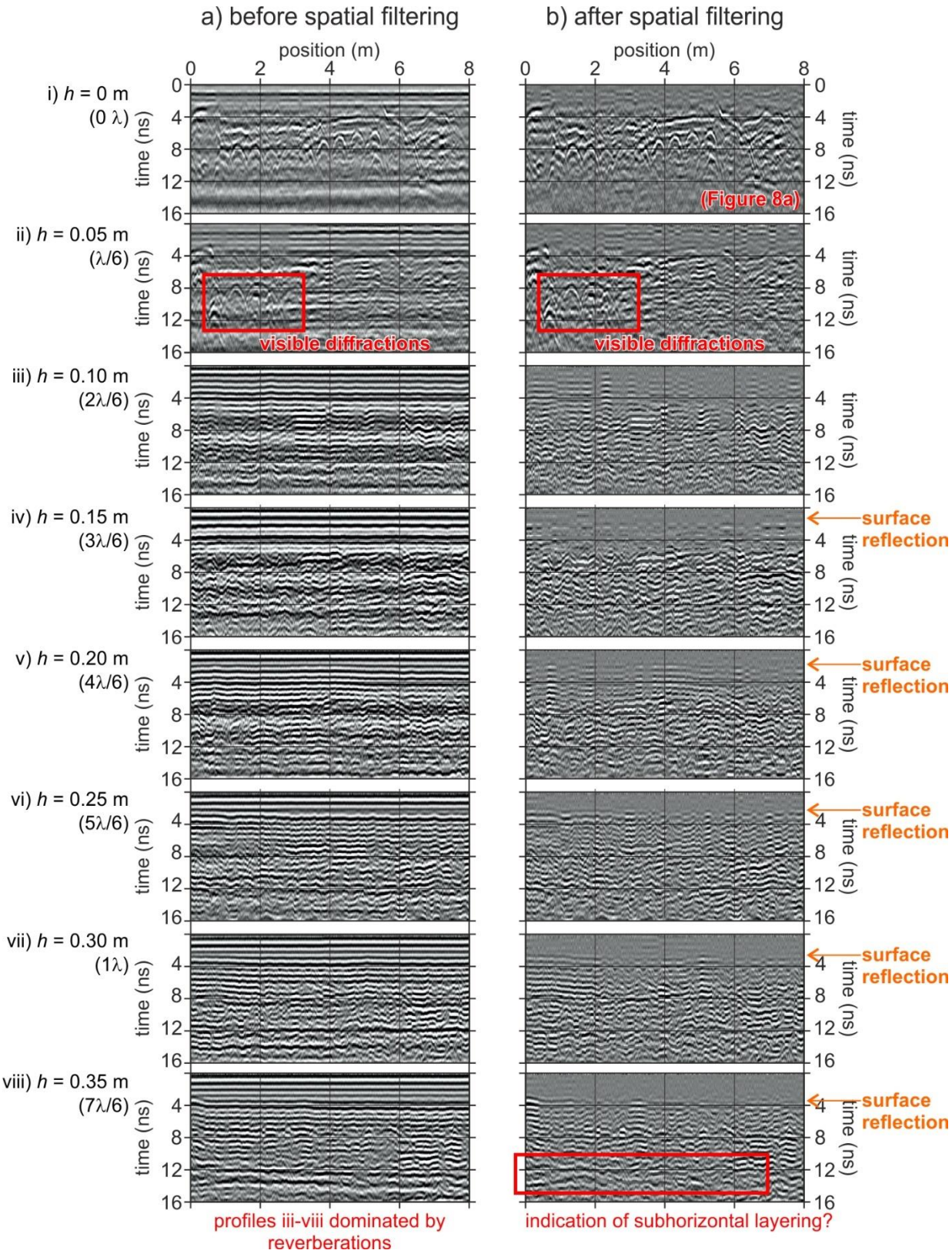

Figure 9. GPR Profiles from Canal Road survey, with *h* increased from (i) 0 m to (viii) 0.35 m (= 7λ/6). Data are shown (a) before and (b) after the application of spatial filtering. Red boxes show the indication of subhorizontal layering for large *h*, and orange annotations highlight the reflection from the ground surface.

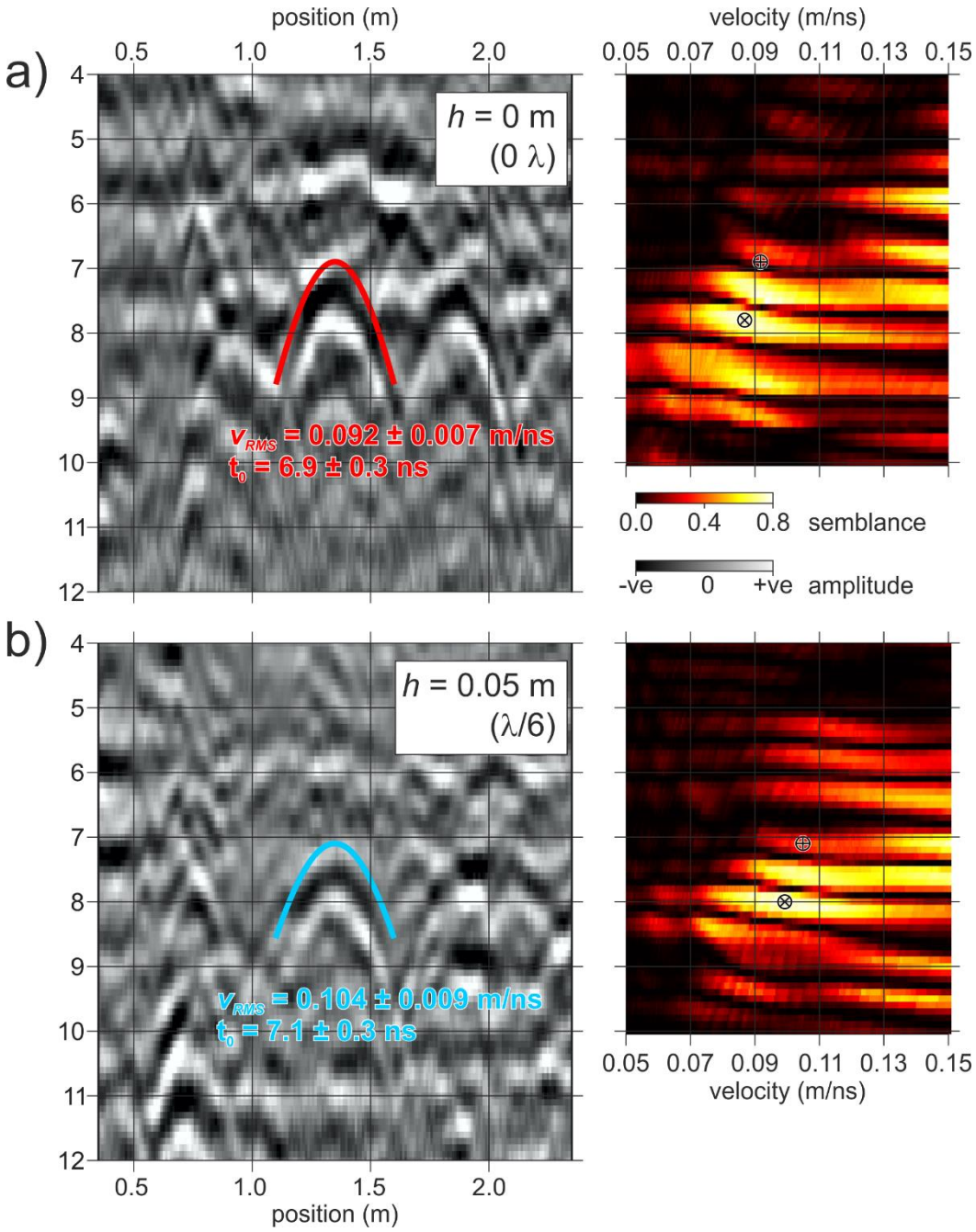

Figure 10. Semblance analysis of diffraction highlighted in Figure 8, for a) ground-based antennas and b) antennas at h = 0.05 m. Diffraction hyperbolae (red) are defined by [v_{RMS}:t_0] shown by ornament ⊕ in the semblance panels, across the 0.25 m aperture either side of the diffraction apex. Annotated velocity precision is based on the width of the 90% semblance contour.

5. Discussion

Drone platforms offer logistical benefits for GPR surveying, but the imaging and analysis of diffraction hyperbolae can be vulnerable to significant errors related to strong refraction effects at the air-ground interface. Recommendations for optimising drone flight-height are contradictory when made using different approaches: ray-based models suggest a 'fly high' strategy to minimise refraction, but a finite-difference scheme indicates that 'flying low' benefits both the precision and accuracy of velocity estimates. Field surveys were designed to explore which guidance was more applicable in practice but, on the whole, our dataset does little to recommend drone-based diffraction imaging at all. Although data quality in our lowest flight-height (0.05 m, $\lambda/6$) compared well with that from a conventional ground-based acquisition, the obscurity of diffractions in the wider dataset suggests that velocity accuracy may be of secondary importance to the question of whether they can be recognised at all. Although higher-order definitions of v_{RMS} (e.g., Causse, 2004) can benefit velocity accuracy, their value could be undermined if no response from the diffracting target can be observed.

Two considerations may explain the disappearance of diffracting responses in the real data. First, Figure 5 showed that characteristic diffraction responses will flatten rapidly with increasing flight-height, to the point where they may become indistinct from subhorizontal reflectivity and, potentially, the reflection from the air-ground interface. With reduced curvature, the diffraction is more vulnerable to further travel-time perturbations related to (e.g.) microtopography on the air-ground interface and/or small-scale velocity anomalies in the overburden. A further feature of our real data was the strong reverberations in the air gap: these were suppressed using spatial filters that preferentially attenuate horizontal trends, hence it is possible that diffraction amplitudes were also attenuated in this step.

The second consideration concerns the spatial resolution of the wavelet, expressed by its Fresnel diameter, F_d,

$$F_d = v_{RMS} (2t_0\tau)^{½}, \qquad (4)$$

where τ is the half-period of the dominant frequency (Lindsey, 1989). For a wavelet of any given frequency, propagating for a fixed travel-time, spatial resolution will be poorer (i.e., F_d increases) for increased v_{RMS}. For the models in Figure 6a, assuming τ = 0.5 ns and flight-height increased from 0 to 0.6 m, v_{RMS} and t_0 increase respectively from ~0.08 to 0.21 m/ns. This leads lead F_d to increase from 0.2 to 0.7 m. The expression of diffracting targets may fundamentally change for drone-based antennas compared to their appearance in a ground-based system. For our real dataset, the

sequence of closely-spaced diffractions may appear as the specular surface in our highest flight-height.

Drone-based GPR applications therefore merit further investigation, but we suggest that they are more likely suitable for imaging specular targets than they are for deriving robust velocity models. Furthermore, there would be adverse consequences for any studying that targeted diffractions, even if they were to be used for entirely qualitative imaging purposes. In some settings, drones may offer greater promise: airborne radar methods are already well-established in glaciology, and the drone-based platform may be less problematic given the small refractive index at the air-snow/ice interface (e.g., Tan, 2018; Mankoff et al., 2020). For more conventional terrestrial settings, if drone imaging is to be undertaken, we would recommend acquiring accompanying ground-based data, both to benchmark any loss of image quality and provide more reliable velocity control.

6. Conclusions

Drone technology offers logistical benefits for several geophysical survey methods, and numerous researchers have explored its applicability for GPR acquisition. Established guidance suggests that the optimal flight height for the antennas is between 0.5-1.5 times the GPR wavelength in air, but no study has to date assessed this recommendation for its impact on diffraction-based velocity analysis. This impact is potentially significant, owing to strong refraction effects at the air-ground interface

Synthetic datasets suggest that velocity analyses are both more accurate and precise if the drone is flown as close to the ground surface as possible. Although this geometry risks stronger ray-bending, the effect of non-hyperbolic terms is minimised by the anisotropic radiation pattern of the GPR antenna. Furthermore, higher flight heights produce flatter diffraction trajectories, risking diffraction responses being overlooked and/or indistinguishable from nearby subhorizontal reflectivity.

A field dataset simulating a drone-based acquisition highlights the vulnerability of diffractions being overlooked. Antennas are raised to over 1 wavelength (0.3 m) from the ground surface, yet diffractions are only visible in the lowest-flying dataset (0.05 m off the ground). A combination of reverberation in the air-gap and a decrease in the horizontal resolution of the wavelet likely explains this poor performance. We conclude that the drone-based platform merits further investigation for GPR applications, but it is likely more suitable for imaging specular reflectivity than it is the quantitative analysis of diffraction responses.

Acknowledgements

TMK undertook the preliminary stages of this research while studying MSc Exploration Geophysics at the University of Leeds. Advice on gprMax simulation from Antonis Giannopoulos was gratefully received.

Data availability

Field data are available to download from the figshare repository available at https://doi.org/10.6084/m9.figshare.16573025.v1.

References

Alkhalifah T (1997). Velocity analysis using non-hyperbolic moveout in transversely isotropic media. Geophysics, 62(6), 1683-2002.

Annan AP and Jackson SR (2017). The WARR Machine. 9th International Workshop on Advanced Ground Penetrating Radar (IWAGPR), Edinburgh, UK, 28-30 June 2017.

Booth A (2021). Profiles of Ground-Penetrating Radar data simulating a drone-mounted acquisition. figshare. Dataset. 10.6084/m9.figshare.16573025.v1

Booth AD, Clark RA and Murray T (2010). Semblance response to a ground-penetrating radar wavelet and resulting errors in velocity analysis. Near Surface Geophysics, 8(3), 235-246.

Booth AD, Clark RA and Murray T (2011). Influences on the resolution of GPR velocity analyses and a Monte Carlo simulation for establishing velocity precision. Near Surface Geophysics, 9(5), 399-411.

Booth AD and Pringle JK (2016). Semblance analysis to assess GPR data from a five-year forensic study of simulated clandestine graves. Journal of Applied Geophysics, 125, 37-44.

Bradford JH, Nichols J, Mikesell TD and Harper JT (2009). Continuous profiles of electromagnetic wave velocity and water content in glaciers: an example from Bench Glacier, Alaska, USA. Annals of Glaciology, 50(51), 1-9.

Causse E (2004). Approximations of reflection travel times with high accuracy at all offsets. Journal of Geophysics and Engineering, 1(1), 28-45. 10.1088/1742-2132/1/1/004

Causse E and Sénéchal P (2006). Model-based automatic dense velocity analysis of GPR field data for the estimation of soil properties. Journal of Geophysics and Engineering, 3(2), 169-176.

Cerquera MRP, Montaño JDC and Mondragón I (2017). UAV for landmine detection using SDR-based GPR technology. In Robots Operating in Hazardous Environments (H Canbolat ed), IntechOpen, Ch 2. 10.5772/intechopen.69738.

Chandra M and Tanzi TJ (2018). Drone-borne GPR design: propagation issues. Comptes Rendus Physique. 19, 72-84. 10.1016/j.chry.2018.01.022.

Diamanti N and Annan P (2017). Air-launched and ground-coupled GPR data. EuCAP2017, 11th European Conference on Antennas and Propagation, Paris, France. 10.23919/EuCap.2017.7928409.

Dix CH (1955). Seismic velocities from surface measurements. Geophysics, 20, 68-86.

Dou Q, Wei L, Magee DR and Cohn AG (2017). Real-time hyperbola recognition and fitting in GPR data. IEEE Transactions on Geoscience and Remote Sensing, 55(1),51-62.

Eriksen A, Gascoyne J and Al-Nuaimy W (2004). Improved productivity and reliability of ballast inspection using road-rail multi-channel GPR. Railway Engineering, 6th-7th July 2004, Commonwealth Institute, London, UK.

Edemsky D, Popov A, Prokopovich I and Garbatsevich (2021). Airborne ground penetrating radar, field test. Remote Sensing, 13, 667. 10.3390/rs13040667.

Hammack R, Veloski G, Schlagenhauf M, Lowe R, Zorn A and Wylie L (2020). Using drone-mounted geophysical sensors to map legacy oil and gas infrastructure. Unconventional Resources Technology Conference, Houston, Texas, USA, URTeC: 2876.

García-Fernández M, Álvarez López Y, Gonazález Valdés B, Rodríguez Vaquiero Y, Las-Heras Andrés F and Pino García A (2018). Synthetic aperture radar imaging system for landmine detection using a ground penetrating radar on board an Unmanned Aerial Vehicle. IEEE Access, 6, 45100-45112. 10.1109/ACCESS.2018.2863572.

García-Fernández M, Álvarez López Y, De Mitri A, Castrillo Martínez D, Á;varez-Narciandi G and Las-Heras Andrés F (2020). Portable and easily-deployable air-launched GPR scanner. Remote Sensing, 12.1833, 10.3390/rs12111833.

Jazayeri S, Klotsche A and Kruuse S (2018). Improved resolution of pipes with full waveform inversion of common-offset GPR data using PEST; Geophysics, 83(4), 1-64.

Lane Jr JW (2019). Development of a drone-deployed ground-penetrating radar system for non-contact bathymetry of freshwater systems. AGU-SEG Airborne Geophysics Workshop, Davie, Florida, 11-13 June.

Lyndsey JP (1989). The Fresnel Zone and its interpretative significance. The Leading Edge, 8(10), 33-39.

Mankoff KD, van As D, Lines A, Bording T, Elliott J, Kraghede R, Cantalloube H, Oriot H, Dubois-Fernandez P, Ruault du Pleiss O, Christiansen AV, Auken E, Hansen K, Colgan W and Karlsson NB (2020). Search and recovery of aircraft parts in ice-sheet crevasse fields using airborne and in situ geophysical sensors. Journal of Glaciology, 66(257), 496-508. 10/1017/jog.2020.26.

Ofcom (2019). Requirements and guidance notes for ground probing and wall probing radar. UK Government Office of Communications, Report OfW 350.

Pieraccini M, Rohjani N and Miccinesi L (2017). Comparison between horn and bow-tie antennas for Ground Penetrating Radar. 9th International Workshop on Advanced Ground Penetrating Radar (IWAGPR), Edinburgh, Scotland. 10.1109/IWAGPR.2017.7996051.

Ristic A, Petrovacki D and Govedarica M (2009). A new method to simultaneously estimate the radius of a cylindrical object and the wave propagation velocity from GPR data. Computers & Geosciences, 35(8), 1620-1630.

Saarenketo T and Scullion T (2000). Road evaluation with ground penetrating radar. Journal of Applied Geophysics, 43(2-4), 119-138. 10.1016/S0926-9851(99)00052-X.

Shihab S and Al-Nuaimy W (2005). Radius estimation for cylindrical objects detected by ground penetrating radar. Subsurface Sensing Technologies and Applications, 6(2), 151-166.

St. Clair J and Holbrook WS (2017). Measuring snow water equivalent from common-offset GPR records through migration velocity analysis. The Cryosphere, 11(6), 2997-3009.

Stucchi E, Ribolini A and Tognarelli A (2020). High-resolution coherency functions for improving the velocity analysis of ground-penetrating radar data. Remote Sensing, 12, 1246.

Šipoš D and Gleich G (2020). A lightweight and low-power UAV-borne ground penetrating radar design for landmine detection. Sensors, 22(2234). 10.3390/s22082234

Tan AE-C, Eccleston K, Platt I, Woodhead I, Rack W and McCulloch J (2018). Microwave measurements of snow over sea-ice in Antarctica. Proceedings of the 12th International Conference on Electromagnetic Wave Interaction with Water and Moist Substances (ISEMA), Lublin, Poland, 2-7 June; Institute of Electrical and Electronic Engineers (IEEE): Piscataway, NJ, USA, 2018, 1-9.

Valentine S (2019). Geophysical trespass, privacy and drones in oil and gas exploration. Journal of Air Law and Commerce, 84(3), Article 6.

1 Warren C and Giannopoulos A (2012). Investigation of the directivity of a commercial ground-
2 penetrating radar antenna using a finite-difference time-domain antenna model. 14th International
3 Conference on Ground Penetrating Radar, 4-8 June, Shanghai, China.

4 Warren C, Giannopoulos A and Giannakis I. (2016). gprMax: Open source software to simulate
5 electromagnetic wave propagation for Ground Penetrating Radar. Computer Physics
6 Communications, 209, 163-170.

7 Zan Y, Li Z, Su G and Zhang X (2016). An innovative vehicle-mounted GPR technique for fast and
8 efficient monitoring of tunnel lining structural conditions. Case Studies in Nondestructive Testing
9 and Evaluation, 6(A), 63-69. 10.1016/j.csndt.2016.10.001.